JGR Space Physics

RESEARCH ARTICLE
10.1029/2024JA033452

Statistical Characterization of Joule Heating Associated With Ionospheric ULF Perturbations Using SuperDARN Data

Xueling Shi[1,2], Shibaji Chakraborty[1,3], Joseph B. H. Baker[1], Michael D. Hartinger[4,5], Wenbin Wang[2], J. Michael Ruohoniemi[1], Dong Lin[2], William Lotko[2,6], Kevin Sterne[1], and Kathryn A. McWilliams[7]

[1]Department of Electrical and Computer Engineering, Virginia Tech, Blacksburg, VA, USA, [2]High Altitude Observatory, National Center for Atmospheric Research, Boulder, CO, USA, [3]Space and Atmospheric Instrumentation Lab, Embry-Riddle Aeronautical University, Daytona Beach, FL, USA, [4]Space Science Institute, Boulder, CO, USA, [5]Department of Earth, Planetary and Space Sciences, University of California Los Angeles, Los Angeles, CA, USA, [6]Thayer School of Engineering, Dartmouth College, Hanover, NH, USA, [7]Institute of Space and Atmospheric Studies, University of Saskatchewan, Saskatoon, SK, Canada

Abstract Ultra low frequency (ULF; 1 mHz - several Hz) waves are key to energy transport within the geospace system, yet their contribution to Joule heating in the upper atmosphere remains poorly quantified. This study statistically examines Joule heating associated with ionospheric ULF perturbations using Super Dual Auroral Radar Network (SuperDARN) data spanning middle to polar latitudes. Our analysis utilizes high-time-resolution measurements from SuperDARN high-frequency coherent scatter radars operating in a special mode, sampling three "camping beams" approximately every 18 s. We focus on ULF perturbations within the Pc5 frequency range (1.6–6.7 mHz), estimating Joule heating rates from ionospheric electric fields derived from SuperDARN data and height-integrated Pedersen conductance from empirical models. The analysis includes statistical characterization of Pc5 wave occurrence, electric fields, Joule heating rates, and azimuthal wave numbers. Our results reveal enhanced electric fields and Joule heating rates in the morning and pre-midnight sectors, even though Pc5 wave occurrences peak in the afternoon. Joule heating is more pronounced in the high-latitude morning sector during northward interplanetary magnetic field conditions, attributed to local time asymmetry in Pedersen conductance and Pc5 waves driven by Kelvin-Helmholtz instability. Pc5 waves observed by multiple camping beams predominantly propagate westward at low azimuthal wave numbers ($|m| < 50$), while high-m waves propagate mainly eastward. Although Joule heating estimates may be underestimated due to assumptions about empirical conductance models and the underestimation of electric fields resulting from SuperDARN line-of-sight velocity measurements, these findings offer valuable insights into ULF wave-related energy dissipation in the geospace system.

Plain Language Summary Ultra low frequency (ULF) waves with frequencies from 1 mHz to several Hz are important for transporting and distributing energy in the near-Earth space environment. Even though scientists have been studying these waves for over a hundred years, there are still important questions about how they affect the upper atmosphere. This study aims to determine how much energy from ULF waves is deposited into the upper atmosphere, particularly in the Pc5 frequency range (1.6–6.7 mHz). We use data from special radars called SuperDARN, which can measure ULF wave-related electric field variations. By analyzing the electric fields and conductivity in the ionosphere — an ionized layer of the atmosphere filled with charged particles — we estimate the amount of heating caused by ULF waves. Our findings show that heating is stronger in the morning and pre-midnight hours, even though most ULF wave activity occurs in the afternoon. In the high-latitude morning region, heating is especially strong when the interplanetary magnetic field points north, likely due to wave effects and uneven conductivity in the ionosphere. These findings provide new insights into how ULF waves transfer and dissipate energy in the near-Earth space environment, improving our understanding of space weather processes.

Key Points:

- Statistics of Joule heating associated with ionospheric ULF perturbations are analyzed using high-time-resolution SuperDARN data
- Two hotspots of large Joule heating are identified, one in the morning sector and another in the pre-midnight sector
- Pc5 waves with low azimuthal wave numbers mostly propagate westward, while high-m waves primarily propagate eastward

Supporting Information:

Supporting Information may be found in the online version of this article.

Correspondence to:

X. Shi,
xueling7@vt.edu

Citation:

Shi, X., Chakraborty, S., Baker, J. B. H., Hartinger, M. D., Wang, W., Ruohoniemi, J. M., et al. (2025). Statistical characterization of joule heating associated with ionospheric ULF perturbations using superDARN data. *Journal of Geophysical Research: Space Physics*, *130*, e2024JA033452. https://doi.org/10.1029/2024JA033452

Received 18 OCT 2024
Accepted 5 MAR 2025

Author Contributions:

Conceptualization: Xueling Shi, Shibaji Chakraborty, Joseph B. H. Baker, Michael D. Hartinger, Wenbin Wang, J. Michael Ruohoniemi, Dong Lin, William Lotko
Data curation: Shibaji Chakraborty, J. Michael Ruohoniemi, Kevin Sterne
Formal analysis: Xueling Shi, Shibaji Chakraborty
Funding acquisition: Xueling Shi, Joseph B. H. Baker, J. Michael Ruohoniemi
Investigation: Xueling Shi, Shibaji Chakraborty, Joseph B. H. Baker, Michael D. Hartinger, Wenbin Wang

1. Introduction

Ultra low frequency (ULF; 1 mHz - several Hz) waves are ubiquitous in the solar-terrestrial environment. They play important roles in transporting and coupling energy throughout the geospace system. Over the past few

Methodology: Xueling Shi, Shibaji Chakraborty, Joseph B. H. Baker, Michael D. Hartinger, Wenbin Wang, J. Michael Ruohoniemi, Dong Lin
Project administration: Xueling Shi
Resources: Xueling Shi, Joseph B. H. Baker, Michael D. Hartinger, Kathryn A. McWilliams
Software: Xueling Shi, Shibaji Chakraborty, Kevin Sterne
Supervision: Xueling Shi
Validation: Xueling Shi, Shibaji Chakraborty
Visualization: Xueling Shi, Shibaji Chakraborty
Writing – original draft: Xueling Shi, Shibaji Chakraborty
Writing – review & editing: Xueling Shi, Shibaji Chakraborty, Joseph B. H. Baker, Michael D. Hartinger, Wenbin Wang, J. Michael Ruohoniemi, Dong Lin, William Lotko, Kathryn A. McWilliams

decades, significant advances have been made in understanding how external sources from the solar wind (e.g., Kelvin-Helmholtz instability (KHI)) and internal sources in the magnetosphere (e.g., particle injections) drive ULF waves. Extensive studies using both ground-based and space-borne measurements have improved our understanding of ULF wave occurrence and driving mechanisms. For instance, band-limited Pc3 (22–100 mHz) pulsations are commonly observed on the dayside, originating from the foreshock and magnetosheath regions (Ponomarenko et al., 2002), while poloidal (radially polarized magnetic field perturbations) Pc4 (7–22 mHz) waves are frequently detected in the afternoon sector, associated with energetic particle injections (Anderson et al., 1990). In contrast, compressional Pc5 (1.6–6.7 mHz) waves are usually observed on the nightside and flanks of the magnetosphere, and they are often linked to local sources such as the drift mirror instability (A. Hasegawa, 1969) and KHI (Lin et al., 2014; Miura, 1984). Externally driven waves are primarily compressional and toroidal modes with low azimuthal wave numbers (low-m), propagating anti-sunward. In contrast, internal sources tend to generate high-m waves that are easily screened by the ionosphere and thus are not detectable by ground magnetometers (Hughes & Southwood, 1976).

Ultra low frequency waves driven by external solar wind sources can accelerate particles in the ring current and radiation belts through drift-bounce resonance (e.g., Zong et al., 2017). They can also be driven by unstable particle distributions in the magnetosphere and dissipate their energy in the upper atmosphere through field line resonances (FLRs) as Joule heating (e.g., Baddeley et al., 2005). However, major questions remain regarding the spatial extent over which ULF waves occur, the conditions that influence their role in energy transport, and the impacts of energy deposition through these waves on the ionosphere-thermosphere (I-T) system. Joule heating is a significant energy source of the upper atmosphere and an important source of uncertainty in the thermosphere's energy budget (Codrescu et al., 1995). Therefore, contributions to Joule heating from rapid or small-to meso-scale fluctuations in ionospheric electric fields or ion drifts, including those induced by ULF waves, are crucial for accurately estimating the thermosphere's energy budget, particularly at high latitudes (e.g., Cousins & Shepherd, 2012; Deng et al., 2009; Matsuo et al., 2021; Verkhoglyadova et al., 2018).

Joule heating occurs due to collisional interactions among electrons, ions, and neutrals (e.g., Richmond & Thayer, 2000; Vasyliūnas & Song, 2005). These species exhibit differential bulk motion, leading to frictional momentum exchange and heating through collisions. The total Joule heating is the sum of the frictional heating contributions from all species. The Joule heating rate can also be derived from magnetohydrodynamic (MHD) equations using $Q_J = \sigma_p \cdot E'^2$, where σ_p is the Pedersen conductivity and E' is the electric field perpendicular to the magnetic field in the neutral wind reference frame. This is expressed as $E' = E + V_n \times B$, where E is the electric field perpendicular to the magnetic field in the inertial reference frame, V_n is the neutral wind velocity, and B is the Earth's magnetic field. Both ground-based coherent and incoherent scatter radars have been utilized to investigate thermospheric Joule heating in general (e.g., Kosch & Nielsen, 1995; Thayer, 1998), as well as its contributions from ULF waves (e.g., Allan & Poulter, 1984; Crowley et al., 1985).

Table 1 summarizes previous research on energy deposition into the I-T system via ULF wave-induced Joule heating using ground-based radar measurements, adapted from Table 2 of Rae et al. (2007). Greenwald and Walker (1980) estimated that energy deposition through Joule heating by Pc5 toroidal mode pulsations could account for up to 4% of the total energy deposition during a small substorm. In contrast, Rae et al. (2007) found that Joule heating from a global FLR event could contribute 30% or more to the total energy deposition during a substorm cycle. These estimates, which vary by five orders of magnitude as shown in Table 1, were mainly based on case studies with limited spatial coverage (only auroral zone radars or a single satellite pass) and temporal coverage (~1 min radar samples). Consequently, these studies required assumptions about wave lifetimes and spatial extent and could not statistically examine higher frequency waves occurring at lower latitudes corresponding to the core of the ring current/radiation belts. Of particular note, the limited case studies in Table 1 show that the total energy deposition through typical high-m waves is on the order of 10^{10} J (Baddeley et al., 2005), much less than through typical low-m waves. However, recent studies have identified a category of high-m poloidal Pc4 waves with long lifetimes, ranging from several hours to days (see Table 1 in Shi, Baker, et al., 2018). These waves, usually observed during the recovery phase of a magnetic storm, show a clear correlation with the Dst index (Archer et al., 2018), suggesting energy transfer from energetic particles to the poloidal ULF waves. These high-m waves can propagate to the ionosphere through FLRs and be detected by ground-based radars and in ionospheric Total Electron Content (TEC) measurements (Shi, Baker, et al., 2018; Zhai et al., 2021), but they are not detectable by ground magnetometers due to ionospheric screening effects (Hughes &

Table 1
Energy Deposition Into the Ionosphere-Thermosphere System via Ultra Low Frequency Wave Joule Heating From Previous Ground-Based Radar Studies

Previous work	Event type	Local dissipation rate [mW/m^2]	Total dissipation rate [W]	Total energy deposition [J]
Greenwald and Walker (1980)	low-m Pc5	4.84	6×10^9	2×10^{13}
Allan and Poulter (1984)	low-m Pc5	-	1.7×10^8	6×10^{11}
	high-m Pc5	-	8.3×10^6	3×10^{10}
Crowley et al. (1985)	low-m Pc5	10 (peak value)	-	4×10^{12}
Baddeley et al. (2005)	high-m Pc5	0.075	2.7×10^6	$\sim 10^{10}$
	giant pulsations	0.68	7.9×10^6	$\sim 10^{11}$
Rae et al. (2007)	low-m Pc5	1.3	9.9×10^9	1.1×10^{15}
van Hazendonk et al. (2024)	low/intermediate m-value Pc5	0.5–3 (base level)	-	1.24×10^{13}

Southwood, 1976). Given their long duration and wide azimuthal spatial extent, these waves likely contribute significantly to Joule heating in the I-T system, especially during the storm recovery phase, when energy deposition due to convection electric field and auroral precipitation is significantly diminished. However, few studies have statistically quantified the wave energy budget in the coupled solar wind-magnetosphere-ionosphere-thermosphere system due to observational limitations. Statistically quantifying the contribution of ULF waves to the global energy budget will provide new insights into the role and relative importance of different types of ULF waves in energy transfer and dissipation in the geospace system.

In addition to radar studies that measure ionospheric electric fields and Joule heating rates, satellite observations have also been used to estimate Joule heating rates and energy deposition more broadly through measurements of wave Poynting flux. Hartinger et al. (2015) estimated ULF wave energy flux into the ionosphere using Time History of Events and Macroscale Interactions during Substorms (THEMIS) satellite observations and found that ULF waves typically make a small contribution to global Joule heating. ULF wave Joule heating rates (integrated over the 3–30 mHz band) generally range from 0.001 to 1 mW/m^2, but can be significant in extreme events ($\geq$ 10 mW/m^2). They also found that ULF waves routinely make significant contributions to local Joule heating rates near the noon and midnight sectors. These results are generally consistent with the average Alfvénic Poynting flux distribution derived from Polar satellite observations (Keiling et al., 2003) and MHD simulations (Zhang et al., 2012). However, it is important to note that Poynting flux does not necessarily equal to Joule heating. Although previous studies have shown that Joule heating is the dominant energy sink for ULF waves (Hartinger et al., 2011; Rae et al., 2007), the energy of a standing Alfvén wave can be converted into particle kinetic energy (e.g., Wright et al., 2003) or propagate down the magnetotail (Mann et al., 1999). Therefore, more direct measurements of ionospheric heating rates using ground-based radars are essential to accurately assess the relative importance of various mechanisms, including determining the extent to which Poynting flux associated with ULF waves contributes to Joule heating.

Incoherent scatter radar (ISR) measurements, such as electron density, electron and ion temperatures, and ion drift velocity, along with derived parameters like neutral wind velocity and Pedersen conductivity, can be used to estimate the Joule heating rate (e.g., van Hazendonk et al., 2024; Thayer, 1998). ISRs offer the advantage of providing altitude profiles of these parameters, enabling the calculation of height-resolved Joule heating rates. However, ISR measurements are limited by the small number of available radars, their restricted spatial coverage, and typically low temporal resolution (e.g., $\geq$1 min). These constraints make it challenging to statistically quantify the Joule heating rate across large spatial scales and capture high frequency ULF wave contributions. In this study, we address these limitations by leveraging high-temporal-resolution camping-beam measurements from a global network of coherent scatter radars to quantify the contribution of ULF waves to energy deposition in the I-T system. Although numerous mechanisms have been proposed to explain the excitation of ULF waves, the relative importance of these drivers in shaping the spatial distribution of waves and their role in energy transfer within the geospace system remain poorly understood. This analysis aims to advance our understanding of the energy transfer and dissipation processes associated with ULF waves, shedding light on their impacts on the geospace environment.

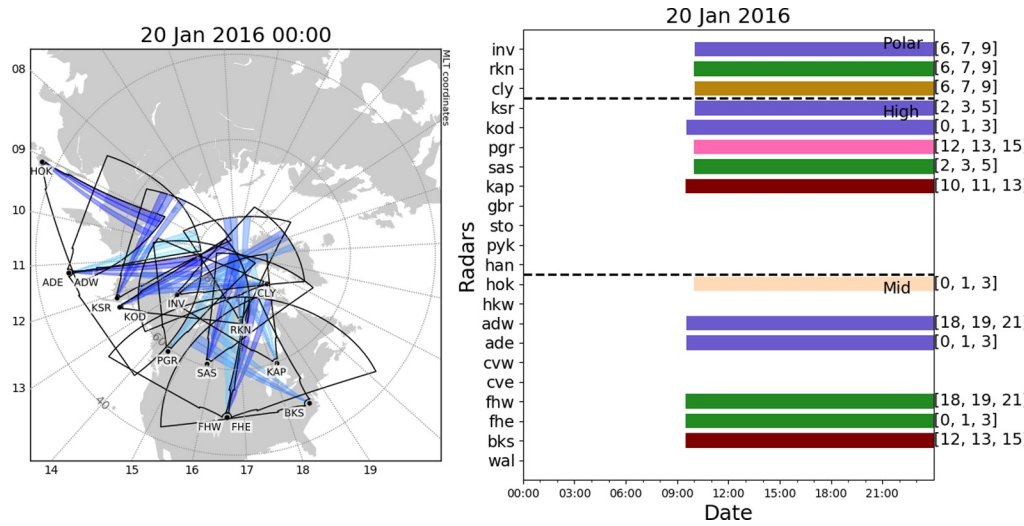

Figure 1. Left: Fields of view of radars operating in the Radiation Belt Storm Probes (RBSP) mode on 20 January 2016. Right: Bar plot showing the time intervals when specific radars were operating in the RBSP mode on 20 January 2016. The numbers on the right of each bar indicate the RBSP mode camping beams of specific radars.

2. Dataset and Models

The Super Dual Auroral Radar Network (SuperDARN) is an international network of over 30 low-power, high-frequency (3–30 MHz) coherent scatter radars located from middle to polar latitudes in both hemispheres that monitor Earth's ionosphere (Chisham et al., 2007; Nishitani et al., 2019). These radars detect Doppler velocity oscillations caused by wave-related electric fields when ULF waves pass through the ionosphere. In their standard operating mode, SuperDARN radars sequentially scan across 16 to 24 beams, with an azimuthal separation of ∼3°. Each beam is subdivided into 75 (or 100) range gates, each spanning 45 km in distance. A full scan, completed in 1–2 min, covers an azimuthal sector of 52° to 78° and extends over 3,000 km in range, providing extensive spatial coverage. For this study, we utilize data from radars operating in the Radiation Belt Storm Probes (RBSP) special mode. This mode, introduced in November 2012 after the launch of the Van Allen Probes (formerly RBSP), utilizes three camping beams sampled at a higher rate of approximately 18 s by interleaving soundings on the camping beams with regular azimuth scans at a 2 min cadence. The RBSP mode continued until September 2017, except for special requests.

Typically, the RBSP mode is scheduled under two conditions: during conjunction with the Van Allen Probes (referred to as rbspscan mode) or when triggered by the Dst index (referred to as rbspscan CT-trig mode). The rbspscan mode is scheduled for SuperDARN radars whose fields of view (FOV) overlay with the ionospheric footprint of one of the Van Allen Probes. The rbspscan CT-trig mode is activated when the Dst index drops below −50 nT and ends when the Dst index rises above −30 nT. While the CT-trig mode may introduce a sampling bias toward moderate to intense geomagnetic activity based on the Dst index, it accounts for only 18% of the total RBSP mode data, with the remaining 82% from the conjunction-based rbspscan mode. Figure S1 in Supporting Information S1 shows histograms of hourly averaged values of (a) Sym-H index, (b) Interplanetary Magnetic Field (IMF) B_y, and (c) IMF B_z for all identified Pc5 wave events (see Section 3 for event detection details). This analysis demonstrates that our database spans a range of geomagnetic activities and IMF conditions, making it well-suited for statistical study.

For ULF wave event detection, we use SuperDARN Line-of-Sight (LoS) Doppler velocity data collected from the three camping beams during the RBSP mode from 2013 to 2017. These measurements, taken from multiple camping beams, can also be used to determine the azimuthal wave number (m-value). SuperDARN data are typically unevenly sampled due to the dependence on backscatter. Sampling rates can vary based on different operating modes and radar configurations. Therefore, pre-processing is necessary to remove noise, bad records, and ground scatter, and to interpolate across data gaps (see next section for more details).

Figure 1 (left) shows an example of the FOV of radars operating in the RBSP mode on 20 January 2016. The bar plot on the right shows the time intervals during which specific radars were operating in the RBSP mode, with the numbers on the right of each bar indicating the camping beams of the radars on that day. Detailed information about the RBSP mode operation from all northern hemisphere radars between 2013 and 2017 is available in the CSV format (see the Open Research section).

Eighteen radars were regularly scheduled to operate in the RBSP mode from 2013 to 2017. It is worth noting that a few radars not operating in this mode on 20 January 2016, are not shown in Figure 1. We excluded data from the Clyde River radar due to a velocity spike issue, possibly related to phase unwrapping caused by the radar's azimuthal orientation. Despite this, the expanded radar coverage at mid-latitudes and high-time-resolution sampling enabled by this mode across middle, high, and polar latitudes allow for new investigations into the spatial extent of inner magnetosphere waves in the Pc4-5 frequency range (2–22 mHz), covering both high- and low-m modes (e.g., Shi, Baker, et al., 2018). These waves could not be routinely studied in this way before due to sparse satellite coverage and the screening of high-m waves in ground magnetometer data.

To estimate the ionospheric electric fields from the LoS velocity data obtained by the SuperDARN radars, the International Geomagnetic Reference Field (IGRF) model (Alken et al., 2021) is used. After the ionospheric electric fields are calculated, we use an empirical solar Extreme UltraViolet (EUV) conductance model (Brekke & Moen, 1993) and the OVATION Prime auroral precipitation model (Newell et al., 2009, 2010) to determine the ionospheric conductance for calculating the Joule heating rate.

3. Methodology

In this section, we outline the methodology used to detect Pc5 ULF waves and extract the associated parameters from SuperDARN RBSP mode measurements. We developed an algorithm for detection of the SuperDARN RBSP mode information including the operating time windows and camping beam numbers of the RBSP modes across all SuperDARN radars located in the northern hemisphere, covering the period from 2013 to 2017. The following steps were taken to identify Pc5 waves in SuperDARN LoS Doppler velocity data, estimate the corresponding Joule heating rates, and calculate the azimuthal wave numbers: (a) pre-processing the data by applying filtering, interpolation, detrending, and generating power spectral density (PSD) using the Fast Fourier Transform (FFT); (b) employing a narrowband wave detection algorithm on the PSD to identify Pc5 wave events; (c) calculating the Joule heating rate for the detected Pc5 wave events by estimating the electric field based on the LoS Doppler velocity and calculating the height-integrated Pedersen conductivity including contributions from solar EUV and auroral precipitation; and (d) calculating the azimuthal wave numbers for the identified Pc5 events.

3.1. Data Processing

In this study, we utilize SuperDARN data from FitACF 3 files, processed using the SuperDARN data analysis software, the Radar Software Toolkit (RST) (SuperDARN Data Analysis Working Group et al., 2022). Power (signal-to-noise ratio), LoS Doppler velocity, and Doppler spectral width of the received backscatter are the primary data products of SuperDARN, stored in FitACF files. These parameters are derived by fitting the complex autocorrelation function (ACF) for each range gate to time lags generated using a multipulse sequence (Greenwald et al., 1985). The spectral width, estimated from the ACF power decorrelation time, is widely used to identify magnetospheric boundaries mapped onto the ionosphere and to distinguish between ionospheric and ground backscatter (Ponomarenko & Waters, 2006). We pre-processed the SuperDARN measurements by applying thresholds to power levels, Doppler velocity, spectral width, ground scatter flags, and errors in Doppler velocity and spectral width, which is a standard procedure for selecting ionospheric backscatter and rejecting ground scatter in SuperDARN data (e.g., Bland et al., 2014). Specifically, we discarded data if (a) the power was below 3 dB, (b) the Doppler velocity was within the range of ±50 m/s, the spectral width was below 50 m/s, or if the ground scatter flag was set, and (c) the errors in Doppler velocity or spectral width exceeded 100 m/s. These criteria remove most noise and ground scatter data so that our analysis can focus on good-quality ionospheric backscatter data that can be used to estimate ionospheric electric fields (e.g., Bland et al., 2014; Shi, Ruohoniemi, et al., 2018). To focus on the F-region ionosphere, approximately 300 km in altitude, where most ionospheric backscatter originates due to field-aligned plasma irregularities, we excluded data with slant ranges less than 500 km (corresponding to the first seven range gate cells). The slant range refers to the distance along the radar

beam from the radar site to the scattering volume in the ionosphere where the backscattered signal is detected. This exclusion effectively removes near-range scatter from meteors and the E-region, allowing the analysis to concentrate on the desired ionospheric region for Joule heating rate calculations.

Since ULF waves are expected to manifest in the LoS Doppler velocity, we detrended the Doppler velocity for each range cell using a 10 min running average to remove the background convection velocity. The 10 min window size was determined through trial and error by Ponomarenko et al. (2003) as the optimal effective window for removing background drift, enhancing the visualization of ULF waves in SuperDARN data. Due to the pre-processing steps outlined in the previous paragraph (e.g., removing noise, bad records, and ground scatter) and the inherent uneven sampling of SuperDARN data caused by variability in backscatter availability, the detrended LoS Doppler velocity data from each 1 hr interval for each range cell must be interpolated to a regular 18 s interval (resulting in 200 data points per hour). This ensures a uniformly sampled time series for subsequent analysis. To further ensure data quality, we discard data from each 1 hr interval if they do not meet the following criteria: (a) the interval contained more than 70% of the expected data points, adjusted for varying radar integration times (2.90–3.75 s); (b) the largest data gap within the hour was less than 6 min; and (c) there were fewer than four data points classified as outliers, defined as being outside six times the median absolute deviation of Doppler velocity in each 1 hr window.

The processed and interpolated LoS Doppler velocities for each 1 hr window once identified as a backscatter event, is then used to calculate the PSD using an FFT. Prior to applying the FFT, a Hanning window was applied to the data to minimize edge effects, smooth the PSD for peak power identification, and ensure reliable phase information for estimating azimuthal wave number.

3.2. Wave Event Detection

After pre-processing and identifying all backscatter events, we apply a Pc5 wave detection algorithm, as described by Takahashi and Ukhorskiy (2007), to identify Pc5 wave signatures in SuperDARN RBSP mode LoS Doppler velocity data. To detect a wave event within each 1 hr interval, we first locate the largest peak in the PSD within the Pc5 frequency band (1.6–6.7 mHz). Next, we verify that the full width at half maximum (FWHM) of the largest PSD peak, which measures the distance between the lower (f_{lower}) and upper (f_{upper}) frequencies at half of the PSD peak's maximum, is less than 2 mHz, and that both f_{lower} and f_{upper} fall within the Pc5 frequency band. If these criteria are satisfied, we compute the Pc5 index (I_{Pc5}), defined as the ratio of spectral power integrated over the Pc5 frequency range to the total spectral power. If I_{Pc5} exceeds 0.6, indicating that at least 60% of the total integrated power lies within the Pc5 frequency range, the event is classified as a Pc5 wave event. Although the majority (>60%) of the processed Doppler velocity is attributed to Pc5 waves, higher-frequency waves (e.g., Pc3-4 waves with frequencies >6.7 mHz) also contribute to the ionospheric electric field and the Joule heating rate derived from the Doppler velocity. Figure 2 presents an example of a wave event, demonstrating the algorithm's effectiveness in detecting Pc5 wave events. The code also generates summary plots, such as those in Figure 2, enabling visual verification of the algorithm's performance.

3.3. Joule Heating Rate Estimation

The Joule heating rate of each identified Pc5 wave event is calculated in three steps. First, we compute the root-mean-square electric fields (E_{rms}) using SuperDARN LoS Doppler velocity measurements (Greenwald & Walker, 1980) and the IGRF geomagnetic field vector. Second, we calculate the ionospheric height-integrated Pedersen conductivity (conductance, Σ_P) using the method described by Cousins et al. (2015), which employs an empirical solar conductance model and the Robinson empirical relationship (Robinson et al., 1987). This approach maps conductance as a function of total electron energy flux and average energy, accounting for three auroral precipitation types (diffuse, monoenergetic, and broadband) based on the OVATION Prime 2010 model, implemented in Python as OVATION Pyme (available at https://github.com/lkilcommons/OvationPyme). Finally, we calculate the height-integrated Joule heating rates (Q_J) for each identified Pc5 wave event using the equation $Q_J = \Sigma_p \cdot E_{rms}^2$. Here, E_{rms} represents the root-mean-square electric field during the Pc5 wave event within the 1 hr interval, computed as $\left(E_{rms} = \sqrt{\overline{E_i^2}}\right)$, where E_i denotes the instantaneous electric fields. The instantaneous electric fields E_i are derived using $E_i = -V_i \times B$, where V_i is the SuperDARN LoS Doppler velocity after processing and detrending, as outlined in subsection 3.1 Data Processing, and B is the IGRF

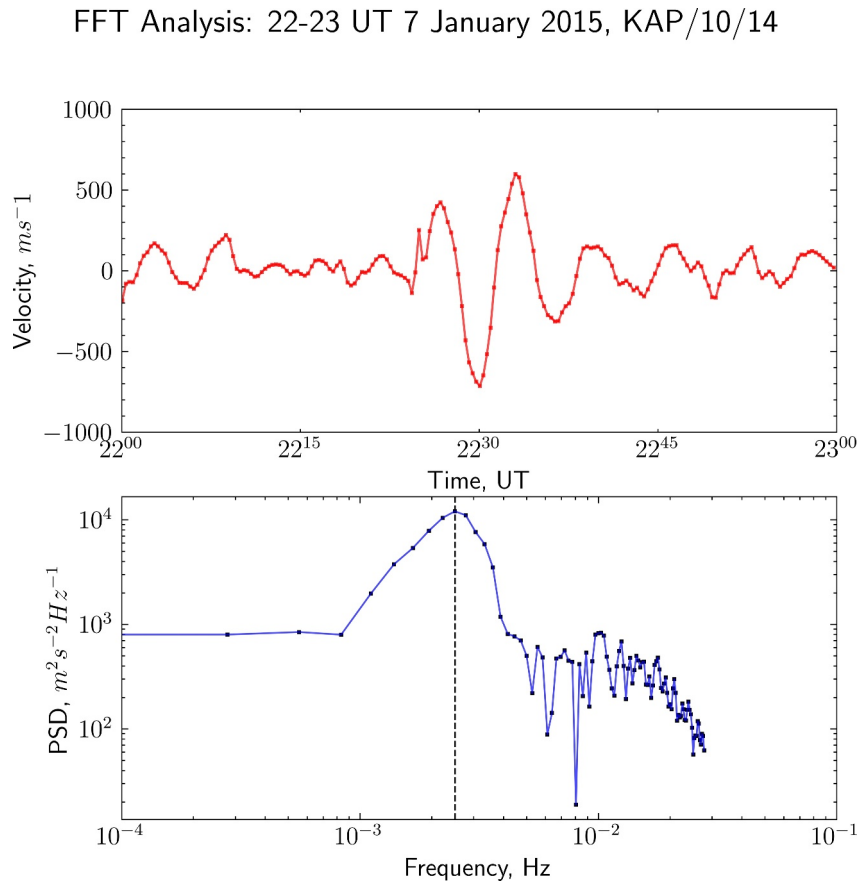

Figure 2. An example event of Pc5 waves detected using the wave detection algorithm. Top: Re-sampled time series of the LoS velocity data from beam 10 and gate 14 of the Kapuskasing (KAP) radar at 22–23 UT on 7 January 2015. Bottom: The power spectral density of the time series shown in the top panel. The dashed black vertical line marks the frequency (2.5 mHz) of a Pc5 wave event detected by the algorithm.

geomagnetic field vector. Note that, when calculating the Joule heating rate in this study, we ignore the effects of the neutral wind ($V_n \times B$) due to the lack of available wind measurements. Furthermore, we exclude the contribution from the large-scale convection electric field, focusing instead on the electric field fluctuations within the ULF wave frequency range. This approach aligns with previous studies that similarly omitted neutral wind effects due to the absence of direct wind measurements (e.g., Baddeley et al., 2005; Rae et al., 2007). It provides an estimate of the energy dissipation in the upper atmosphere during the 1 hr interval of an identified Pc5 wave event.

3.4. Azimuthal Wave Number Calculation

The azimuthal wave number (m-value) is calculated using a method similar to that described by James et al. (2013). Specifically, for Pc5 wave events identified by the same radar during the same time interval but at different locations (i.e., different range gates), we select measurements from similar L-shells (within 1° of magnetic latitude (MLAT)) that are separated in the azimuthal direction (magnetic longitude separation ≥1°). To calculate the m-value, we require that at least three events meet all criteria, including having the same wave frequency. A linear fit is then applied to the wave phases and magnetic longitudes to determine the azimuthal wave number. A negative m-value indicates westward propagation, while a positive m-value indicates eastward propagation. This algorithm was applied to all Pc5 wave events detected by northern hemisphere SuperDARN radars operating in the RBSP mode during 2013–2017.

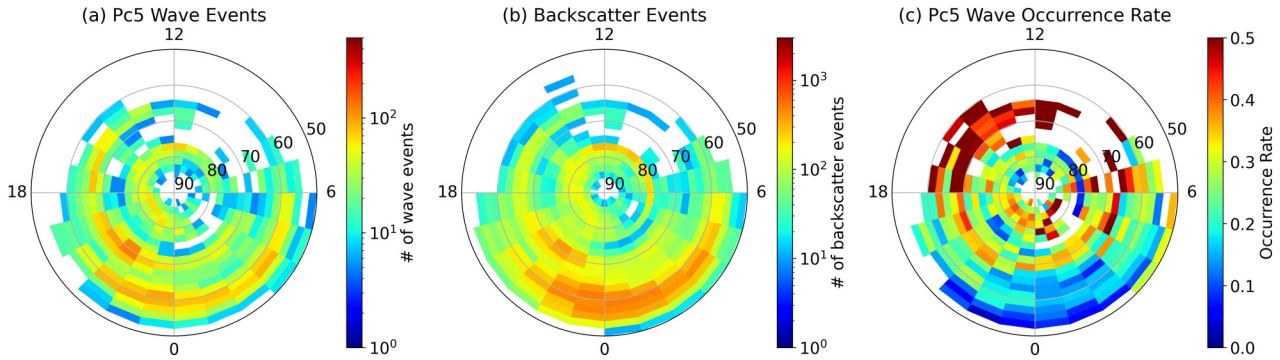

Figure 3. Magnetic latitude-magnetic local time maps of (a) Pc5 wave occurrence, (b) ionospheric backscatter occurrence, and (c) Pc5 wave occurrence rate.

4. Statistical Results

4.1. ULF Wave Occurrence Spatial Distribution

After identifying the Pc5 wave events and backscatter events using the methods described in the previous section, we can analyze the statistics of ULF wave occurrence. Figure 3 shows the occurrence of (a) Pc5 wave events, (b) backscatter events, and (c) the occurrence rate of Pc5 wave events, calculated as the ratio of (a) to (b), displayed in MLAT and magnetic local time (MLT) maps. Each bin in the map represents 2° in MLAT and 1 hr in MLT. The backscatter events indicate data coverage, shown in the middle panel, including events with at least 70% valid ionospheric backscatter echoes after removing all noise, bad records, and spikes within a 1 hr interval. In addition, we require a minimum of 10 backscatter events per bin to be included in the distribution analysis (Figure 3b), leaving bins with fewer than 10 events blank, indicating insufficient data coverage. Figures 3a and 3b illustrates the Pc5 event and data coverage provided by three tiers of radars at polar (MLAT ≥75°), high (75° > MLAT ≥ 65°), and middle latitudes (65° > MLAT ≥ 50°), as shown in Figure 1(left). Ionospheric backscatter covers most MLTs in the polar region and is predominantly observed on the nightside at midlatitudes, extending into the afternoon sector at high latitudes, as shown in Figure 3b. The overall Pc5 wave event occurrence rate is 23% with 8,769 Pc5 wave events identified out of a total of 37,747 backscatter events. The highest occurrence rates are observed at 60–70° MLAT in the afternoon sector as shown in Figure 3c, consistent with findings in Shi, Ruohoniemi, et al. (2018) using 6 s SuperDARN THEMIS mode data. Although some bins with high occurrence rates in this sector may be influenced by low counts of wave and backscatter events, the overall trend of elevated occurrence rates in the afternoon sector remains consistent with expectations and is physically meaningful.

4.2. Wave Electric Field and Joule Heating Spatial Distribution

The root-mean-square electric field (E_{rms}) is calculated using the SuperDARN LoS velocity and the IGRF geomagnetic field for the 8,769 identified Pc5 events. The mean value of the E_{rms} in each bin is shown in Figure 4a. Due to limited coverage of Pc5 events below 60° MLAT (Figure 3a), we only present maps for regions

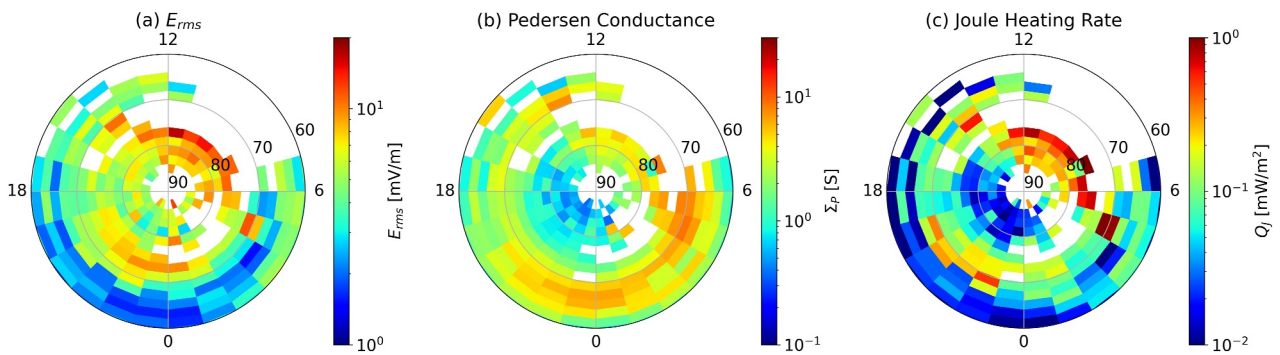

Figure 4. Magnetic latitude-magnetic local time maps showing the mean values of (a) root-mean-square electric field (E_{rms}), (b) Pedersen conductance (Σ_P), and (c) Joule heating rate (Q_J) for all identified Pc5 wave events.

above 60° MLAT in Figure 4. To calculate the mean value, we require at least 5 events in each bin, resulting in more blank bins on the dayside where ionospheric backscatter and wave events are less frequent compared to Figure 3. Comparing Figure 3c with Figure 4a, we observe that high wave occurrence rates do not always correspond to large ionospheric electric fields. While the highest occurrence rates are observed at 60–70° MLAT in the afternoon sector (Figure 3c), large wave electric fields are concentrated at 75–85° MLAT in the morning sector and 70–80° MLAT in the pre-midnight sector (Figure 4a). The mean E_{rms} of the 8,769 identified Pc5 events is 5.2 mV/m, with a median E_{rms} of 3.9 mV/m. For reference, the mean E_{rms} of all backscatter events is 4.5 mV/m, and the median is 2.9 mV/m. The spatial distribution of mean ionospheric electric fields is generally consistent with the findings of Cousins and Shepherd (2012), who statistically characterized the small-scale spatial (45–450 km) and temporal (2–20 min) electric field variability using SuperDARN data. They found that the magnitudes of both temporal and spatial variability peak in the auroral zone (~70°–80°) and on the dayside near noon in MLT. However, our study reveals a distinct local time asymmetry, with a preference for the morning and pre-midnight sectors.

Figure 4b shows the mean height-integrated Pedersen conductivity (conductance) for all identified Pc5 wave events in each MLAT-MLT bin. Blank bins in the morning sector indicate data gaps due to limited Pc5 wave event coverage in that region. The highest Pedersen conductance appears in the dawn sector, centered around 70° MLAT, with generally high conductance extending to the pre-midnight sector between 62 and 72° MLAT. Our conductance map may differ from empirical conductance models (e.g., Hardy et al., 1987), as it represents a mixture of different seasons, geomagnetic conditions, and periods of high Pc5 wave power observed by the SuperDARN radars. If the conductance map is separated by season, higher Pedersen conductance is observed on the dayside during summer (not shown). Additionally, SuperDARN data coverage (Figure 3b) is influenced by ionospheric irregularities, which vary with local time and season, potentially introducing a bias by favoring conditions that support ionospheric backscatter, especially during periods of low sunlight (e.g., more dayside high-latitude events during local winter).

The spatial distribution of wave Joule heating rates (Figure 4c) is similar to the wave electric field distribution (Figure 4a), with notable hotspots in the pre-noon and pre-midnight sectors. However, Joule heating rates are more pronounced at slightly lower latitudes due to the Pedersen conductance distribution (Figure 4b), which is generally stronger at lower latitudes in the auroral zone, particularly at night. The mean (median) Joule heating rate for the 8,769 identified Pc5 wave events is 0.10 (0.02) mW/m^2, consistent with the typical range of ULF wave Joule heating rates (0.001–1 mW/m^2) implied from THEMIS satellite observations by Hartinger et al. (2015). Notably, there is a gap in data coverage on the dayside (white regions, primarily in the morning sector) below 76° MLAT, above which both wave electric fields and Joule heating rates peak. This apparent peak at 76–78° MLAT may not be real, as enhanced wave electric fields and Joule heating rates could extend to lower latitudes on the dayside, where SuperDARN ionospheric backscatter coverage is limited. Additionally, many large electric field events occur at very high latitudes (>80° MLAT), most likely within the polar cap region, where Joule heating rates remain low due to low conductance in that region. Note that we also examined the median value distributions of wave electric field, Pedersen conductance, and Joule heating rate. The spatial patterns observed are similar to those of the mean value distributions presented in Figure 4.

Figure 5 further explores the dependencies on MLAT and local time by categorizing events into two MLAT groups: $MLAT \geq 75°$ (high latitudes, Figures 5a–5d) and $65° \leq MLAT < 75°$ (middle latitudes, Figures 5e–5h). Figures 5a and 5e show the Pc5 wave occurrence as histograms, while Figures 5b–5d and 5f–5h display box-and-whisker plots for Pedersen conductance (Σ_P), root-mean-square electric field (E_{rms}), and Joule heating rate (Q_J), organized into 2 hr MLT bins. The red line within each box represents the median value for each MLT bin. The boxes represent the interquartile range (IQR), spanning from the 25th percentile (Q1) to the 75th percentile (Q3), encompassing the central 50% of the data. Whiskers extend from the boxes to the smallest and largest values within 1.5 times the IQR. The use of box plots effectively highlights the variability and distribution of each parameter across MLT, offering a clear comparison of central tendencies and spread between the two latitude groups.

In the high-latitude group ($MLAT \geq 75°$), the MLT coverage is generally good, except for the two post-midnight bins (2–6 hr MLT) where fewer than 100 events are recorded (Figure 5a). The box-and-whisker plots in Figures 5b–5d indicate that dayside Pedersen conductance, wave electric fields, and Joule heating rates are significantly higher than those on the nightside, with a pronounced morning-afternoon asymmetry where all three

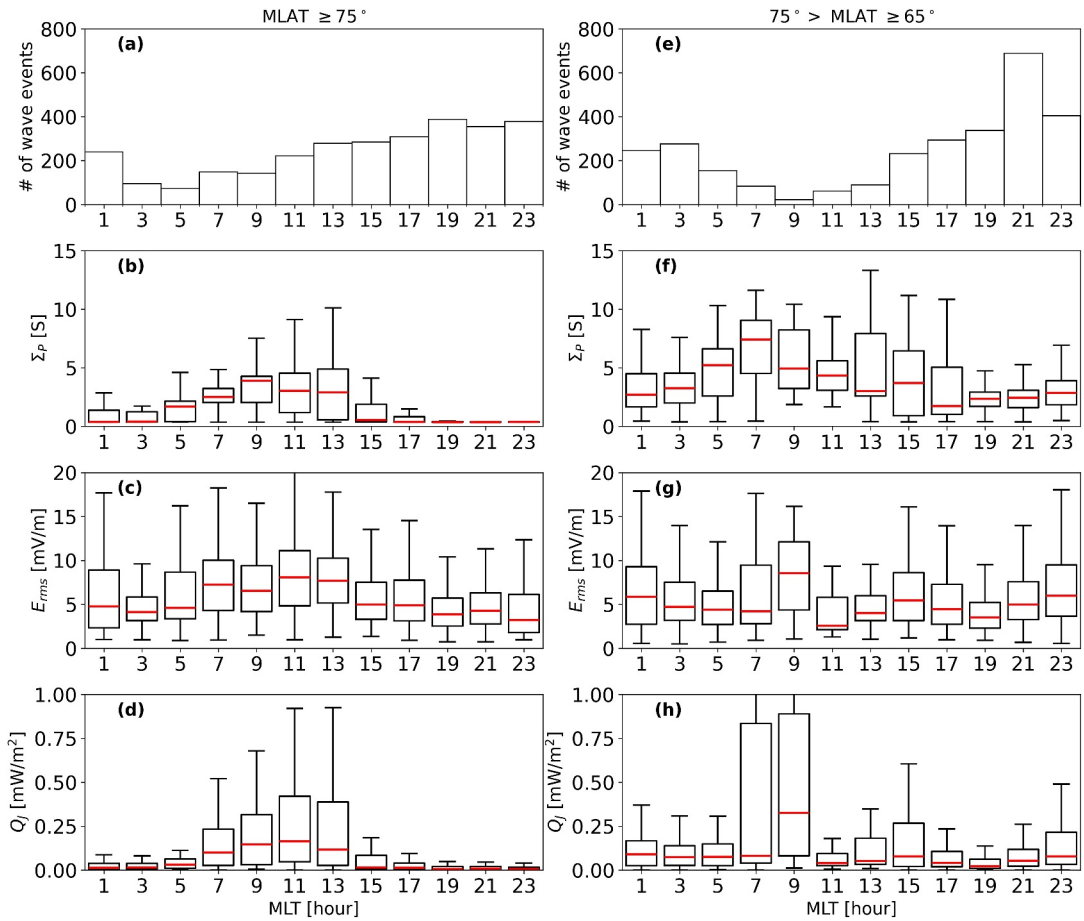

Figure 5. Magnetic local time (MLT) distribution of parameters associated with Pc5 wave events at $MLAT \geq 75°$ (left column) and $75° > MLAT \geq 65°$ (right column). Panels (a/e) show histograms of Pc5 wave occurrences. Box-and-whisker plots of (b/f) Pedersen conductance (Σ_P), (c/g) root-mean-square electric field (E_{rms}), and (d/h) Joule heating rate (Q_J) associated with Pc5 wave events are shown for each MLT bin. In the box-and-whisker plots, red lines mark the median values, while the boxes represent the interquartile range (IQR), covering the 25th to 75th percentiles (Q1 to Q3). Whiskers extend to the smallest and largest values within 1.5 times the IQR.

parameters are stronger in the morning sector, consistent with the patterns in Figure 4. For the middle-latitude group ($65° \leq MLAT < 75°$), Figures 5e–5h reveal the MLT dependence of wave events, although many dayside bins (6–14 hr MLT) have limited data coverage (Figure 5e). The Pedersen conductance at middle latitudes (Figure 5f) is generally larger than at high latitudes (Figure 5b) across most MLT bins. Additionally, there is a noticeable minimum around dusk in Pedersen conductance (Figure 5f), wave electric fields (Figure 5g), and Joule heating rate (Figure 5h), followed by increasing values toward midnight and afternoon. However, due to insufficient dayside data coverage (Figure 5e), the observed enhancement of Joule heating rate (Figure 5h), characterized by a large IQR (indicating a large spread and variability in the middle 50% of the data), in the dawn-to-morning sector (6–10 hr MLT) requires further verification.

4.3. IMF Dependence of ULF Wave Ionospheric Energy Deposition

The pre-midnight electric field and Joule heating hotspot is well-understood as being driven by magnetotail dynamo processes (e.g., Lotko et al., 2014; Zhang et al., 2014), but the high-latitude morning sector hotspot remains more enigmatic. Figures 4 and 5 indicate that this phenomenon results from the combined effects of enhanced wave electric fields and Pedersen conductance in the morning sector. Initially, one might speculate that the preference for strong electric fields and Joule heating in the morning sector may be related to IMF conditions. To explore this, we analyzed high-latitude events ($MLAT \geq 75°$) under different IMF conditions to assess their relationship.

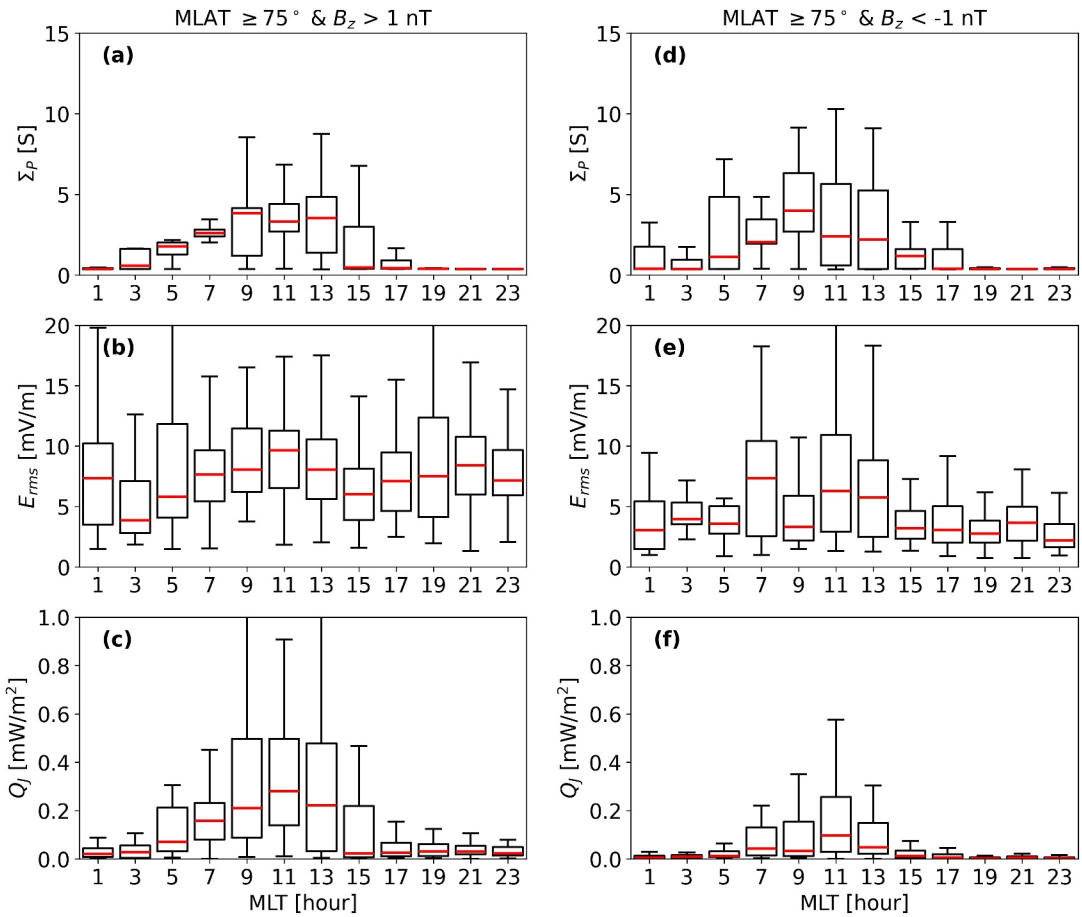

Figure 6. Magnetic local time (MLT) distribution shown in box-and-whisker plots for (a) Pedersen conductance (Σ_P), (b) root-mean-square electric field (E_{rms}), and (c) Joule heating rate for events at $MLAT \geq 75°$ during $B_z > 1nT$ conditions, and for (d) Pedersen conductance (Σ_P), and (e) root-mean-square electric field (E_{rms}), and (f) Joule heating rate for events at $MLAT \geq 75°$ during $B_z < -1nT$ conditions. The red line within each box represents the median value for each MLT bin.

The effect of IMF B_z is presented in Figure 6, which presents the variations of Σ_P, E_{rms}, and Q_J for events at $MLAT \geq 75°$, displayed as a function of MLT in box-and-whisker plots for $B_z > 1nT$ (left column) and $B_z < -1nT$ (right column). Pedersen conductance does not exhibit a significant change with the sign of IMF B_z, with a prominent pre-noon enhancement evident in both conditions (Figure 6 top panels). However, Pc5 wave electric fields are notably stronger during northward IMF (Figure 6b) compared to southward IMF (Figure 6e), leading to a significant increase in Joule heating rates on the dayside during northward IMF conditions (Figure 6c) compared to southward IMF (Figure 6f). Further analysis of IMF B_y dependence (see Figure S2 in Supporting Information S1) reveals that Pedersen conductance, electric fields, and Joule heating rates are enhanced in the pre-noon sector under both IMF B_y polarities ($B_y > 1nT$ and $B_y < -1nT$), though the effect is more pronounced during dawnward IMF ($B_y < -1nT$). The enhancement of electric field in the pre-noon sector may be associated with the positioning of the convection throat, typically located in this area regardless of IMF B_y polarity (e.g., Heppner & Maynard, 1987; Weimer, 1995). While IMF conditions mainly affect wave electric field distribution on the dayside, the sustained enhanced Joule heating rates in the morning sector under various IMF conditions suggest that increased conductance, likely due to diffuse auroral precipitation, plays a critical role.

4.4. Large Joule Heating Event Spatial Distribution

To determine the spatial distribution of large Joule heating events, Figure 7 presents scatter plots of events with Joule heating rates exceeding 1.00 mW/m^2. We identify 129 (~1.5%) large Joule heating rate events with a mean (maximum) Joule heating rate of 2.35 (25.43) mW/m^2 and a mean (maximum) E_{rms} of 19.17 (65.05) mV/m.

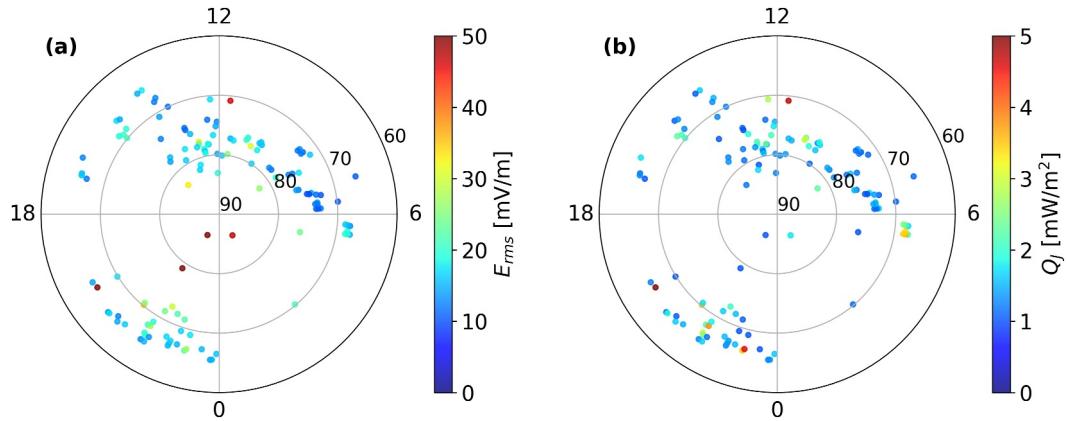

Figure 7. Scatter plots of (a) E_{rms}, and (b) Joule heating rate (Q_J) in magnetic latitude-magnetic local time coordinates for 129 events with Joule heating rate greater than 1 mW/m^2.

These events are concentrated on the dayside at about 70–80° MLAT and in the pre-midnight sector at 65–70° MLAT. The dayside high-latitude electric field (Figure 7a) and Joule heating (Figure 7b) enhancement is likely associated with the cusp and low-latitude boundary layer regions, where downward particle precipitation and Poynting flux occur, leading to enhanced ionosphere conductivity and Joule heating. The pre-midnight events located at lower latitudes are most likely linked with substorm activity, where particle injections and internally driven high-m waves are prevalent.

4.5. Wave Propagation and Azimuthal Spatial Scale

Ultra low frequency waves can be driven either externally by solar wind disturbances or internally by instabilities within the magnetosphere. Externally driven waves generally propagate anti-sunward with low azimuthal wave number (m-value) and have large spatial extent. In contrast, internally driven waves typically propagate sunward with higher m-values and more localized spatial extents. A key advantage of SuperDARN RBSP mode data is its ability to estimate the m-value, which is essential for understanding the driving mechanisms and spatial characteristics of ULF waves. To calculate the azimuthal wave number, measurements must be taken at a roughly constant L-shell but separated azimuthally (James et al., 2013). Using this method, we identified 391 events with reliable m-value estimates, mostly range from −50 to 50, as shown in the histogram in Figure 8a. Negative m-

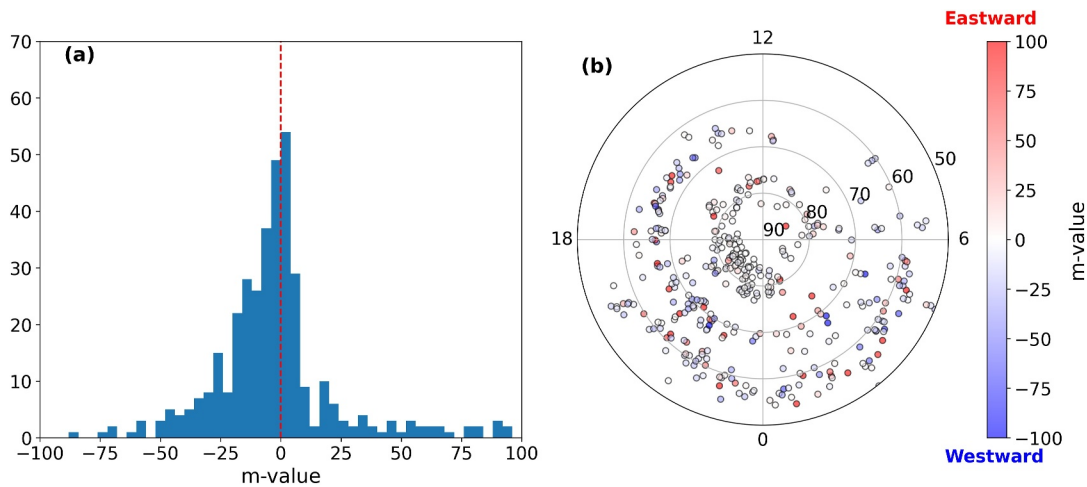

Figure 8. (a) Histogram showing the distribution of azimuthal wave number (m-value), and (b) scatter plot representing the m-value distribution in the magnetic latitude-magnetic local time coordinates. The dashed red vertical line indicates an m-value of 0. Negative m-values (blue dots) indicate westward propagation, while positive m-values (red dots) denote eastward propagation.

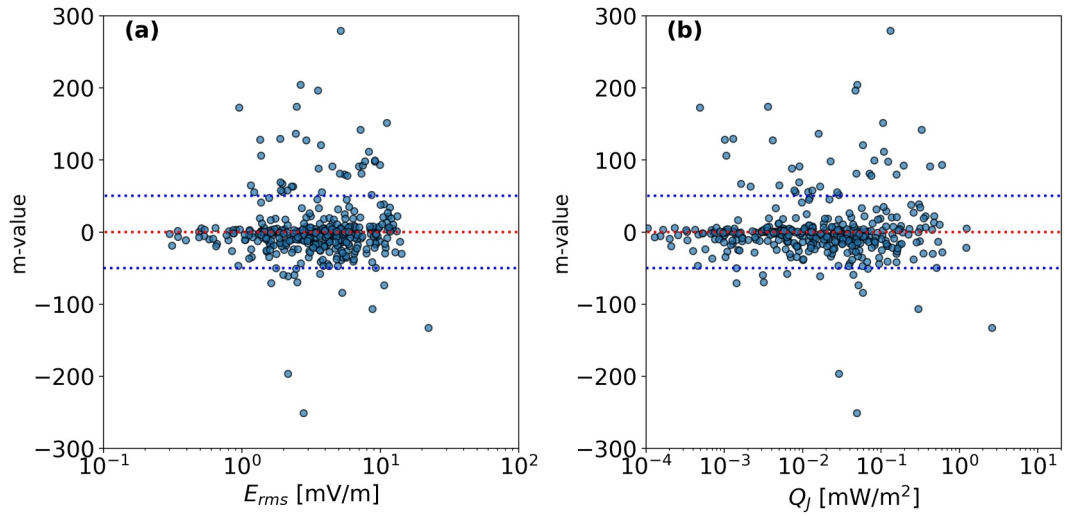

Figure 9. Scatter plots of azimuthal wave number (m-value) versus (a) E_{rms},and (b) Joule heating rate. The dashed red horizontal line indicates an m-value of 0. The dashed blue horizontal lines mark m-values of ±50.

values indicate westward propagation, while positive m-values denote eastward propagation. The histogram is skewed toward negative m-values, indicating a higher occurrence of westward-propagating waves.

The spatial distribution of these events, color-coded by m-values, is shown in Figure 8b. Pc5 events detected by multiple camping beams are concentrated in the afternoon and pre-midnight sectors at MLAT ≥65°, likely observed by high- and polar-latitude radars (see Figure 1 for radar FOV coverage). Events at lower latitudes (<65° MLAT) occur primarily on the nightside and are mostly detected by mid-latitude radars. Events below 70° MLAT tend to have larger m-values (dark blue and red dots), compared to those at higher latitudes (light blue and red dots). The westward-propagating (sunward in the afternoon-to-midnight sectors) events with negative m-values (blue dots) may be driven by internal wave-particle interactions, possibly linked to particle injections from the magnetotail. Some high-m events propagate eastward (red dots) in the afternoon and the night sectors, likely driven by eastward-drifting electrons or external sources, such as magnetosheath high-speed jets or foreshock transients (e.g., Wang et al., 2020).

To examine the relationship between azimuthal wave number and both wave electric field and Joule heating rate, scatter plots of m-values versus (a) E_{rms} and (b) Q_J are presented in Figure 9. No clear dependence between the wave electric field or Joule heating rate and m-value is observed, as both low- and high-m waves contribute to a wide range of electric field strengths and Joule heating rates. It is interesting to note that most high-m ($|m|>50$) events are eastward-propagating (positive m-values), whereas low-m ($|m|<50$) events are predominantly westward-propagating, consistent with the patterns observed in Figure 8. In addition, the contribution of high-m Pc5 waves to local Joule heating rates remains relatively small (mostly < 1 mW/m^2), in agreement with previous case studies (e.g., Baddeley et al., 2005). However, some high-m waves exhibit long lifetimes and wide azimuthal extents, persisting for hours to days during the recovery phase of geomagnetic storms (see Table 1 in Shi, Baker, et al., 2018). While their local Joule heating rates may be small, these long-lived waves could contribute significantly to global Joule heating in the upper atmosphere. To fully quantify their contribution, future studies should include numerical simulations and detailed event analyses that integrate ULF wave properties constrained by multi-point space-borne and ground-based observations.

5. Discussion

This study provides a statistical analysis of ULF wave energy deposition using SuperDARN data and empirical conductance models, including their spatial distribution, dependence on local time, IMF, and azimuthal wave number. Our findings indicate distinct patterns and drivers for ULF wave energy dissipation in the ionosphere, emphasizing the role of Pc5 ionospheric electric fields under northward IMF conditions and their morning sector preference at high latitudes.

The prevalence of Pc5 waves during northward IMF and their morning sector preference in this study may be attributed to the KHI (H. Hasegawa et al., 2003; Henry et al., 2017). Takahashi et al. (2012) noted Pc5 wave occurrence and amplitude enhancement pre-noon with latitude dependence particularly during high-speed solar wind streams, suggesting the KHI caused these features. However, the dependence of Pc5 wave electric fields and Joule heating rates on solar wind speed in this study (not shown) is less pronounced compared to what has been reported in prior studies. Besides wave electric fields, the Pedersen conductance plays a significant role. Newell et al. (2009) identified the dominance of diffuse aurora, which accounts for 84% of energy flux into the ionosphere under low solar wind driving conditions. They also highlight a dayside number flux dominance of diffuse aurora during northward IMF conditions which can be linked to a thicker low-latitude boundary layer during northward IMF (H. Hasegawa et al., 2004). Shue et al. (2001) observed a positive correlation between auroral brightness and solar EUV-produced Pedersen conductance in the early morning sector. These studies indicate combined effects of ionospheric electric field perturbations and diffuse aurora-induced conductance asymmetry in local time, contributing to the observed morning sector enhancement of the Joule heating rate in our study.

Compared to earlier statistical studies on ULF wave occurrence or ionospheric electric field temporal and spatial variability using SuperDARN data (e.g., Cousins & Shepherd, 2012; Shi, Ruohoniemi, et al., 2018), this study, which focuses on ULF wave energy deposition in the upper atmosphere via Joule heating, reveals new insights into the interaction between Alfvénic Poynting flux and ionospheric dynamics. Our results generally align with satellite-based Poynting flux studies by Keiling et al. (2003, 2019), who reported ULF wave energy flux in the Pc3-4 frequency range (6–167 mHz) and extreme Poynting flux also in the dayside high latitude region and nightside. Hartinger et al. (2015) found that ULF wave energy flux, integrated over the 3–30 mHz band, peaks in the postnoon sector based on THEMIS satellite observations. However, due to the high altitude of the spacecraft orbit, it could not differentiate between electromagnetic and particle energy flux. Our study suggests that more of the electromagnetic energy flux measured by THEMIS was probably converted to particle kinetic energy flux before arriving at the ionosphere in the afternoon sector compared to the morning sector. Additionally, Hartinger et al. (2015) only considered measurements when the satellite was inside the magnetopause, whereas this study includes ionospheric regions mapping to locations both inside and outside the magnetopause. Damiano et al. (2007) found that about 30% of a standing Alfvén wave's energy is converted to particle kinetic energy, with the remaining energy contributing to Joule heating, depending on the perpendicular wavelength. Using Europen Incoherent Scatter Scientific Association data, van Hazendonk et al. (2024) determined that kinetic and electromagnetic energy rates (Joule and frictional heating rates) are of similar magnitude and should both be included in energy deposition by ULF waves in the upper atmosphere. It is crucial to emphasize the differences between past studies in predicting where the energy flux “hot spots” should be. When comparing different studies, there are notable differences depending on whether they report only the large amplitude events, averages across all events, the wave frequency band used, and other factors. This variability underscores the complexity of accurately determining energy flux distribution in the ionosphere. Our findings reinforce the importance of Pc5 ULF wave energy deposition in the upper atmosphere via Joule heating, particularly during northward IMF conditions on the dayside.

It is important to note that several factors could affect our results, including ionospheric conductivity, SuperDARN radar geometry, and sampling bias. The height-integrated Pedersen conductivity, derived from empirical solar irradiance and auroral precipitation models, may be underestimated, as these models might not fully capture meso-scale or localized auroral features. Additionally, as demonstrated by Tu et al. (2011), thermosphere heating is both dynamic and height-dependent, with heating rates potentially exceeding quasi-steady-state values by more than a factor of two. Consequently, our Joule heating rate estimation, which relies on empirical height-integrated steady-state conductance, is likely further underestimated. Besides, our analysis can only resolve wave events with spatial scales larger than 45 km (one radar range gate) and temporal scales greater than 18 s (the sampling rate), excluding contributions from smaller spatial and temporal scale waves. More importantly, our estimates of ionospheric wave electric fields, derived from a single component of plasma velocity (LoS Doppler velocity), represent a lower bound on the total electric field magnitude. This approach introduces a limitation in the calculation of Joule heating, as the full vector nature of the electric field is not captured. While two-dimensional ion drift measurements would enhance the accuracy of ionospheric electric field estimations, such data are generally unavailable due to the inherent constraints of single radar systems, including both coherent and incoherent scatter radars. It is also important to note that although our study spans the 2013 to 2017 period, which falls within a solar maximum, the particular solar maximum was one of the quietest in recent times, with few

major geomagnetic storms (e.g., Kp ≥ 8). As a result, the Joule heating estimates in this study are likely lower than what would be expected during more intense geomagnetic storms (e.g., the May 2024 storm). Therefore, our Joule heating rate estimates are conservative.

Furthermore, ionospheric backscatter, particularly on the dayside, tends to occur more frequently during equinox and winter seasons, with reduced coverage in summer (Ruohoniemi & Greenwald, 1997; Shi, Ruohoniemi, et al., 2018). Consequently, the high-latitude dayside results are more representative of conditions in seasons other than summer, while the nightside results are less affected by this seasonal bias. This potential skew underscores the need for caution when generalizing our findings across different seasons. However, despite these conservative estimates and sampling limitations, our results suggest that the actual energy deposition from ULF waves may be even more significant than reported here, underscoring the importance of continued research in this area.

6. Conclusions

In this study, we examined the statistics of Pc5 ULF wave occurrence, electric field, and Joule heating using 5 years (2013–2017) of SuperDARN RBSP mode data. Our findings highlight the important role of ULF waves in I-T energy deposition through Joule heating, particularly in the morning and pre-midnight sectors. Here are the main conclusions from our study.

1. The occurrence of Pc5 waves peaks in the afternoon sector, but the most intense Pc5 wave-related electric fields and Joule heating rates are found in the morning and pre-midnight regions.
2. The enhancement of the Joule heating rate in the morning sector is attributed to the local time asymmetry in Pedersen conductance and the presence of Pc5 waves driven by the KHI.
3. The majority of Pc5 wave events have a Joule heating rate of less than 1.0 mW/m^2, with a mean value of 0.1 mW/m^2 across 8,769 identified events. Events with high Joule heating rate (> 1.0 mW/m^2) are concentrated in the dayside high latitude regions (70–80° MLAT) and in the pre-midnight sector at 65–70° MLAT.
4. Pc5 waves observed by multiple camping beams predominantly propagate westward at low azimuthal wave numbers ($|m| < 50$), while high-m waves are mainly eastward-propagating.

These findings underscore the importance of Pc5 ULF waves in influencing the I-T dynamics. By enhancing our understanding of the spatial and temporal distribution of wave-induced Joule heating, this study provides observational implications for modeling of space weather impacts on Earth's upper atmosphere. Furthermore, our results highlight the need for future research that incorporates more extensive measurements of these waves, particularly during major geomagnetic storms and spacecraft-ground conjugate observations, to further improve our understanding of their space weather effects.

Data Availability Statement

Super Dual Auroral Radar Network (SuperDARN) rawacf data files are available at https://www.frdr-dfdr.ca/repo/collection/superdarn. SuperDARN data has been processed using the RST (https://zenodo.org/records/7467337) developed by the SuperDARN Data Analysis Working Group (SuperDARN Data Analysis Working Group et al., 2022) and accessed by the pyDARN package (https://zenodo.org/records/6473574) developed by the SuperDARN Data Visualization Working Group (Shi et al., 2022; SuperDARN Data Visualization Working Group et al., 2022). The OVATION Pyme Python package is available at https://github.com/lkilcommons/OvationPyme. The majority of analysis and visualization was completed with the help of free, open-source software tools such as numpy (Harris et al., 2020), scipy (Virtanen et al., 2020), matplotlib (Hunter, 2007), IPython (Perez & Granger, 2007), pandas (McKinney, 2010), and others (e.g., Millman & Aivazis, 2011). To parallelize the code we have used Ray, which is a python-based distributed network (Moritz et al., 2018). Our code is published in the Zenodo repository (Chakraborty & Shi, 2024), which contains the Python code, parameters in a Java Script Object Notation (JSON) file, and RBSP mode details from all Northern hemisphere radars between 2013 and 2017 in CSV file format.

Acknowledgments
We acknowledge Gang Lu from High Altitude Observatory for the internal review. XS was supported by National Aeronautics and Space Administration (NASA) awards 80NSSC21K1677 and 80NSSC21K1683, National Science Foundation (NSF) awards AGS-1935110, AGS-2025570, and AGS-2307205. SC was supported by NSF awards AGS-1935110 and AGS-2412294 and NASA awards 80NSSC21K1677 and 80NSSC20K1380. MDH was supported by NASA awards 80NSSC21K1677 and 80NSSC21K1683 and NSF award AGS-2307204. DL and WW were supported by NASA HSR award 80NSSC21K1677, NASA CGS award 80NSSC22M0163 and NASA LWS Grant 80NSSC21K0008. DL was also supported by NASA Grants 80NSSC23K1055 and 80NSSC22K1635. We acknowledge the use of SuperDARN data. Super Dual Auroral Radar Network is a network of radars funded by national scientific funding agencies of Australia, Canada, China, France, Italy, Japan, Norway, South Africa, the United Kingdom, and the United States of America. This research was supported by the International Space Science Institute (ISSI) in Bern, through ISSI International Team project #546 "Magnetohydrodynamic Surface Waves at Earth's Magnetosphere (and Beyond)" and ISSI International Team project #553 "CSES and Swarm Investigation of the Generation Mechanisms of Low Latitude Pi2 Waves".

References

Alken, P., Thébault, E., Beggan, C. D., Amit, H., Aubert, J., Baerenzung, J., et al. (2021). International Geomagnetic Reference Field: The thirteenth generation. *Earth Planets and Space*, *73*, 1–25. https://doi.org/10.1186/s40623-020-01288-x

Allan, W., & Poulter, E. (1984). The spatial structure of different ULF pulsation types: A review of STARE radar results. *Reviews of Geophysics*, *22*(1), 85–97. https://doi.org/10.1029/rg022i001p00085

Anderson, B., Engebretson, M., Rounds, S., Zanetti, L., & Potemra, T. (1990). A statistical study of Pc 3–5 pulsations observed by the AMPTE/CCE magnetic fields experiment, 1. occurrence distributions. *Journal of Geophysical Research*, *95*(A7), 10495–10523. https://doi.org/10.1029/ja095ia07p10495

Archer, M., Hartinger, M., Redmon, R., Angelopoulos, V., Walsh, B. M., & Students, E. H. S. Y. P. (2018). First results from sonification and exploratory citizen science of magnetospheric ULF waves: Long-lasting decreasing-frequency poloidal field line resonances following geomagnetic storms. *Space Weather*, *16*(11), 1753–1769. https://doi.org/10.1029/2018sw001988

Baddeley, L. J., Yeoman, T. K., Wright, D. M., Trattner, K. J., & Kellet, B. J. (2005). On the coupling between unstable magnetospheric particle populations and resonant high m ULF wave signatures in the ionosphere. *Annales Geophysicae*, *23*(2), 567–577. Retrieved from https://doi.org/10.5194/angeo-23-567-2005

Bland, E. C., McDonald, A. J., Menk, F. W., & Devlin, J. C. (2014). Multipoint visualization of ULF oscillations using the Super Dual Auroral Radar Network. *Geophysical Research Letters*, *41*(18), 6314–6320. Retrieved from https://doi.org/10.1002/2014GL061371

Brekke, A., & Moen, J. (1993). Observations of high latitude ionospheric conductances. *Journal of Atmospheric and Terrestrial Physics*, *55*(11), 1493–1512. (The XX IUGG General Assembly) Retrieved from https://doi.org/10.1016/0021-9169(93)90126-J

Chakraborty, S., & Shi, X. (2024). shibaji7/HSR_ULF_Wave_Analysis: HSR joule heating paper [Software]. *Zenodo*. Retrieved from https://doi.org/10.5281/zenodo.13892009

Chisham, G., Lester, M., Milan, S. E., Freeman, M. P., Bristow, W. A., Grocott, A., et al. (2007). A decade of the Super Dual Auroral Radar Network (SuperDARN): Scientific achievements, new techniques and future directions. *Surveys in Geophysics*, *28*(1), 33–109. Retrieved from https://doi.org/10.1007/S10712-007-9017-8

Codrescu, M. V., Fuller-Rowell, T. J., & Foster, J. C. (1995). On the importance of E-field variability for Joule heating in the high-latitude thermosphere. *Geophysical Research Letters*, *22*(17), 2393–2396. Retrieved from https://doi.org/10.1029/95GL01909

Cousins, E. D. P., Matsuo, T., & Richmond, A. D. (2015). Mapping high-latitude ionospheric electrodynamics with SuperDARN and AMPERE. *Journal of Geophysical Research: Space Physics*, *120*(7), 5854–5870. Retrieved from https://doi.org/10.1002/2014JA020463

Cousins, E. D. P., & Shepherd, S. G. (2012). Statistical characteristics of small-scale spatial and temporal electric field variability in the high-latitude ionosphere. *Journal of Geophysical Research*, *117*(A3), A03317. Retrieved from https://doi.org/10.1029/2011JA017383

Crowley, G., Wade, N., Waldock, J., Robinson, T., & Jones, T. (1985). High time-resolution observations of periodic frictional heating associated with a Pc5 micropulsation. *Nature*, *316*(6028), 528–530. https://doi.org/10.1038/316528a0

Damiano, P., Wright, A., Sydora, R., & Samson, J. (2007). Energy dissipation via electron energization in standing shear Alfvén waves. *Physics of Plasmas*, *14*(6). https://doi.org/10.1063/1.2744226

Deng, Y., Maute, A., Richmond, A. D., & Roble, R. G. (2009). Impact of electric field variability on Joule heating and thermospheric temperature and density. *Geophysical Research Letters*, *36*(8), L08105. Retrieved from https://doi.org/10.1029/2008GL036916

Greenwald, R., Baker, K., Hutchins, R., & Hanuise, C. (1985). An HF phased-array radar for studying small-scale structure in the high-latitude ionosphere. *Radio Science*, *20*(1), 63–79. Retrieved from https://doi.org/10.1029/RS020i001p00063

Greenwald, R., & Walker, A. (1980). Energetics of long period resonant hydromagnetic waves. *Geophysical Research Letters*, *7*(10), 745–748. https://doi.org/10.1029/gl007i010p00745

Hardy, D. A., Gussenhoven, M. S., Raistrick, R., & McNeil, W. J. (1987). Statistical and functional representations of the pattern of auroral energy flux, number flux, and conductivity. *Journal of Geophysical Research*, *92*(A11), 12275–12294. Retrieved from https://doi.org/10.1029/JA092iA11p12275

Harris, C. R., Millman, K. J., van der Walt, S. J., Gommers, R., Virtanen, P., Cournapeau, D., et al. (2020). Array programming with NumPy. *Nature*, *585*(7825), 357–362. Retrieved from https://doi.org/10.1038/s41586-020-2649-2

Hartinger, M., Angelopoulos, V., Moldwin, M. B., Glassmeier, K.-H., & Nishimura, Y. (2011). Global energy transfer during a magnetospheric field line resonance. *Geophysical Research Letters*, *38*(12). Retrieved from https://doi.org/10.1029/2011GL047846

Hartinger, M., Moldwin, M. B., Zou, S., Bonnell, J. W., & Angelopoulos, V. (2015). ULF wave electromagnetic energy flux into the ionosphere: Joule heating implications. *Journal of Geophysical Research: Space Physics*, *120*(1), 494–510. Retrieved from https://doi.org/10.1002/2014JA020129

Hasegawa, A. (1969). Drift mirror instability in the magnetosphere. *The Physics of Fluids*, *12*(12), 2642–2650. https://doi.org/10.1063/1.1692407

Hasegawa, H., Fujimoto, M., Maezawa, K., Saito, Y., & Mukai, T. (2003). Geotail observations of the dayside outer boundary region: Interplanetary magnetic field control and dawn-dusk asymmetry. *Journal of Geophysical Research*, *108*(A4). Retrieved from https://doi.org/10.1029/2002JA009667

Hasegawa, H., Fujimoto, M., Saito, Y., & Mukai, T. (2004). Dense and stagnant ions in the low-latitude boundary region under northward interplanetary magnetic field. *Geophysical Research Letters*, *31*(6). Retrieved from https://doi.org/10.1029/2003GL019120

Henry, Z. W., Nykyri, K., Moore, T. W., Dimmock, A. P., & Ma, X. (2017). On the dawn-dusk asymmetry of the Kelvin-Helmholtz instability between 2007 and 2013. *Journal of Geophysical Research: Space Physics*, *122*(12), 11888–11900. Retrieved from https://doi.org/10.1002/2017JA024548

Heppner, J. P., & Maynard, N. C. (1987). Empirical high-latitude electric field models. *Journal of Geophysical Research*, *92*(A5), 4467–4489. Retrieved from https://doi.org/10.1029/JA092iA05p04467

Hughes, W., & Southwood, D. (1976). The screening of micropulsation signals by the atmosphere and ionosphere. *Journal of Geophysical Research*, *81*(19), 3234–3240. https://doi.org/10.1029/ja081i019p03234

Hunter, J. D. (2007). Matplotlib: A 2D graphics environment. *Computing in Science & Engineering*, *9*(3), 90–95. Retrieved from https://doi.org/10.1109/MCSE.2007.55

James, M. K., Yeoman, T. K., Mager, P. N., & Klimushkin, D. Y. (2013). The spatio-temporal characteristics of ULF waves driven by substorm injected particles. *Journal of Geophysical Research: Space Physics*, *118*(4), 1737–1749. Retrieved from https://doi.org/10.1002/jgra.50131

Keiling, A., Thaller, S., Wygant, J., & Dombeck, J. (2019). Assessing the global Alfvén wave power flow into and out of the auroral acceleration region during geomagnetic storms. *Science Advances*, *5*(6), eaav8411. https://doi.org/10.1126/sciadv.aav8411

Keiling, A., Wygant, J., Cattell, C., Mozer, F., & Russell, C. (2003). The global morphology of wave poynting flux: Powering the aurora. *Science*, *299*(5605), 383–386. https://doi.org/10.1126/science.1080073

Kosch, M. J., & Nielsen, E. (1995). Coherent radar estimates of average high-latitude ionospheric Joule heating. *Journal of Geophysical Research*, *100*(A7), 12201–12215. Retrieved from https://doi.org/10.1029/95JA00821

Lin, D., Wang, C., Li, W., Tang, B., Guo, X., & Peng, Z. (2014). Properties of Kelvin-Helmholtz waves at the magnetopause under northward interplanetary magnetic field: Statistical study. *Journal of Geophysical Research: Space Physics*, *119*(9), 7485–7494. https://doi.org/10.1002/2014ja020379

Lotko, W., Smith, R. H., Zhang, B., Ouellette, J. E., Brambles, O. J., & Lyon, J. G. (2014). Ionospheric control of magnetotail reconnection. *Science*, *345*(6193), 184–187. Retrieved from https://doi.org/10.1126/science.1252907

Mann, I. R., Wright, A. N., Mills, K. J., & Nakariakov, V. M. (1999). Excitation of magnetospheric waveguide modes by magnetosheath flows. *Journal of Geophysical Research*, *104*(A1), 333–353. https://doi.org/10.1029/1998ja900026

Matsuo, T., Fan, M., Shi, X., Miller, C., Ruohoniemi, J. M., Paul, D., & Lee, T. C. M. (2021). Multiresolution modeling of high-latitude ionospheric electric field variability and impact on Joule heating using SuperDARN data. *Journal of Geophysical Research: Space Physics*, *126*(9), e2021JA029196. Retrieved from https://doi.org/10.1029/2021JA029196

McKinney, W. (2010). Data structures for statistical computing in Python. In S. van der Walt & J. Millman (Eds.), *Proceedings of the 9th python in science conference* (pp. 56–61). Retrieved from https://doi.org/10.25080/Majora-92bf1922-012

Millman, K. J., & Aivazis, M. (2011). Python for scientists and engineers. *Computing in Science and Engineering*, *13*(2), 9–12. Retrieved from https://doi.org/10.1109/MCSE.2011.36

Miura, A. (1984). Anomalous transport by magnetohydrodynamic Kelvin-Helmholtz instabilities in the solar wind-magnetosphere interaction. *Journal of Geophysical Research*, *89*(A2), 801–818. Retrieved from https://doi.org/10.1029/JA089iA02p00801

Moritz, P., Nishihara, R., Wang, S., Tumanov, A., Liaw, R., Liang, E., et al. (2018). Ray: A distributed framework for emerging AI applications.

Newell, P. T., Sotirelis, T., & Wing, S. (2009). Diffuse, monoenergetic, and broadband aurora: The global precipitation budget. *Journal of Geophysical Research*, *114*(A9). Retrieved from https://doi.org/10.1029/2009JA014326

Newell, P. T., Sotirelis, T., & Wing, S. (2010). Seasonal variations in diffuse, monoenergetic, and broadband aurora. *Journal of Geophysical Research*, *115*(A3). Retrieved from https://doi.org/10.1029/2009JA014805

Nishitani, N., Ruohoniemi, J. M., Lester, M., Baker, J. B. H., Koustov, A. V., Shepherd, S. G., et al. (2019). Review of the accomplishments of mid-latitude Super Dual Auroral Radar Network (SuperDARN) HF radars. *Progress in Earth and Planetary Science*, *6*(1), 27. Retrieved from https://doi.org/10.1186/s40645-019-0270-5

Perez, F., & Granger, B. E. (2007). Ipython: A system for interactive scientific computing. *Computing in Science & Engineering*, *9*(3), 21–29. Retrieved from https://doi.org/10.1109/MCSE.2007.53

Ponomarenko, P. V., Fraser, B. J., Menk, F. W., Ables, S. T., & Morris, R. J. (2002). Cusp-latitude Pc3 spectra: Band-limited and power-law components. *Annales Geophysicae*, *20*(10), 1539–1551. Retrieved from https://doi.org/10.5194/angeo-20-1539-2002

Ponomarenko, P. V., Menk, F. W., & Waters, C. L. (2003). Visualization of ULF waves in SuperDARN data. *Geophysical Research Letters*, *30*(18). Retrieved from https://doi.org/10.1029/2003GL017757

Ponomarenko, P. V., & Waters, C. L. (2006). Spectral width of SuperDARN echoes: Measurement, use and physical interpretation. *Annales Geophysicae*, *24*(1), 115–128. Retrieved from https://doi.org/10.5194/angeo-24-115-2006

Rae, I. J., Watt, C. E. J., Fenrich, F. R., Mann, I. R., Ozeke, L. G., & Kale, A. (2007). Energy deposition in the ionosphere through a global field line resonance. *Annales Geophysicae*, *25*(12), 2529–2539. Retrieved from https://doi.org/10.5194/angeo-25-2529-2007

Richmond, A., & Thayer, J. (2000). Ionospheric electrodynamics: A tutorial. *Magnetospheric current systems*, *118*, 131–146.

Robinson, R. M., Vondrak, R. R., Miller, K., Dabbs, T., & Hardy, D. (1987). On calculating ionospheric conductances from the flux and energy of precipitating electrons. *Journal of Geophysical Research*, *92*(A3), 2565–2569. Retrieved from https://doi.org/10.1029/JA092iA03p02565

Ruohoniemi, J. M., & Greenwald, R. A. (1997). Rates of scattering occurrence in routine HF radar observations during solar cycle maximum. *Radio Science*, *32*(3), 1051–1070. https://doi.org/10.1029/97RS00116

Shi, X., Baker, J. B. H., Ruohoniemi, J. M., Hartinger, M. D., Murphy, K. R., Rodriguez, J. V., et al. (2018). Long-lasting poloidal ULF waves observed by multiple satellites and high-latitude SuperDARN radars. *Journal of Geophysical Research: Space Physics*, *123*(10), 8422–8438. Retrieved from https://doi.org/10.1029/2018JA026003

Shi, X., Ruohoniemi, J. M., Baker, J. B. H., Lin, D., Bland, E. C., Hartinger, M. D., & Scales, W. A. (2018). Survey of ionospheric Pc3-5 ULF wave signatures in SuperDARN high time resolution data. *Journal of Geophysical Research: Space Physics*, *123*(5), 4215–4231. Retrieved from https://doi.org/10.1029/2017JA025033

Shi, X., Schmidt, M., Martin, C. J., Billett, D. D., Bland, E., Tholley, F. H., et al. (2022). pyDARN: A python software for visualizing SuperDARN radar data. *Frontiers in Astronomy and Space Sciences*, *9*, 1022690. https://doi.org/10.3389/fspas.2022.1022690

Shue, J.-H., Newell, P. T., Liou, K., & Meng, C.-I. (2001). The quantitative relationship between auroral brightness and solar EUV Pedersen conductance. *Journal of Geophysical Research*, *106*(A4), 5883–5894. Retrieved from https://doi.org/10.1029/2000JA003002

SuperDARN Data Analysis Working Group, Thomas, E. G., Reimer, A. S., Bland, E. C., Burrell, A. G., Grocott, A., et al. (2022). Superdarn Radar Software Toolkit (RST) 5.0 (v5.0) [Software]. *Zenodo*. Retrieved from https://doi.org/10.5281/zenodo.7467337

SuperDARN Data Visualization Working Group, Schmidt, M. T., Martin, C. J., Shi, X., Tholley, F., Billett, D. D., et al. (2022). Superdarn/pydarn: Pydarn v3.0 (v3.0) [Software]. *Zenodo*. Retrieved from https://doi.org/10.5281/zenodo.6473574

Takahashi, K., & Ukhorskiy, A. Y. (2007). Solar wind control of Pc5 pulsation power at geosynchronous orbit. *Journal of Geophysical Research*, *112*(A11). Retrieved from https://doi.org/10.1029/2007JA012483

Takahashi, K., Yumoto, K., Claudepierre, S. G., Sanchez, E. R., Troshichev, O. A., & Janzhura, A. S. (2012). Dependence of the amplitude of Pc5-band magnetic field variations on the solar wind and solar activity. *Journal of Geophysical Research*, *117*(A4). Retrieved from https://doi.org/10.1029/2011JA017120

Thayer, J. P. (1998). Height-resolved Joule heating rates in the high-latitude E region and the influence of neutral winds. *Journal of Geophysical Research*, *103*(A1), 471–487. Retrieved from https://doi.org/10.1029/97JA02536

Tu, J., Song, P., & Vasyliūnas, V. M. (2011). Ionosphere/thermosphere heating determined from dynamic magnetosphere-ionosphere/thermosphere coupling. *Journal of Geophysical Research*, *116*(A9). Retrieved from https://doi.org/10.1029/2011JA016620

van Hazendonk, C. M., Baddeley, L., Laundal, K. M., & Chau, J. L. (2024). Detection and energy dissipation of ULF waves in the polar ionosphere: A case study using the EISCAT radar. *Journal of Geophysical Research: Space Physics*, *129*(7), e2024JA032633. Retrieved from https://doi.org/10.1029/2024JA032633

Vasyliūnas, V. M., & Song, P. (2005). Meaning of ionospheric Joule heating. *Journal of Geophysical Research*, *110*(A2). Retrieved from https://doi.org/10.1029/2004JA010615

Verkhoglyadova, O. P., Meng, X., Mannucci, A. J., & McGranaghan, R. M. (2018). Semianalytical estimation of energy deposition in the ionosphere by monochromatic Alfvén waves. *Journal of Geophysical Research: Space Physics*, *123*(6), 5210–5222. Retrieved from https://doi.org/10.1029/2017JA025097

Virtanen, P., Gommers, R., Oliphant, T. E., Haberland, M., Reddy, T., Cournapeau, D., et al., SciPy 1.0 Contributors. (2020). SciPy 1.0: Fundamental algorithms for scientific computing in Python. *Nature Methods*, *17*(3), 261–272. https://doi.org/10.1038/s41592-019-0686-2

Wang, B., Liu, T., Nishimura, Y., Zhang, H., Hartinger, M., Shi, X., et al. (2020). Global propagation of magnetospheric Pc5 ULF waves driven by foreshock transients. *Journal of Geophysical Research: Space Physics*, *125*(12), e2020JA028411. Retrieved from https://doi.org/10.1029/2020JA028411

Weimer, D. R. (1995). Models of high-latitude electric potentials derived with a least error fit of spherical harmonic coefficients. *Journal of Geophysical Research*, *100*(A10), 19595–19607. Retrieved from https://doi.org/10.1029/95JA01755

Wright, A. N., Allan, W., & Damiano, P. A. (2003). Alfvén wave dissipation via electron energization. *Geophysical Research Letters*, *30*(16). https://doi.org/10.1029/2003gl017605

Zhai, C., Shi, X., Wang, W., Hartinger, M. D., Yao, Y., Peng, W., et al. (2021). Characterization of high-m ULF wave signatures in GPS TEC data. *Geophysical Research Letters*, *48*(14), e2021GL094282. Retrieved from https://doi.org/10.1029/2021GL094282

Zhang, B., Lotko, W., Brambles, O., Damiano, P., Wiltberger, M., & Lyon, J. (2012). Magnetotail origins of auroral Alfvénic power. *Journal of Geophysical Research*, *117*(A9). Retrieved from https://doi.org/10.1029/2012JA017680

Zhang, B., Lotko, W., Brambles, O., Xi, S., Wiltberger, M., & Lyon, J. (2014). Solar wind control of auroral Alfvénic power generated in the magnetotail. *Journal of Geophysical Research: Space Physics*, *119*(3), 1734–1748. Retrieved from https://doi.org/10.1002/2013JA019178

Zong, Q., Rankin, R., & Zhou, X. (2017). The interaction of ultra-low-frequency Pc3-5 waves with charged particles in Earth's magnetosphere. *Reviews of Modern Plasma Physics*, *1*, 1–90. https://doi.org/10.1007/s41614-017-0011-4